Nano Research

Open Access

Research Article

Superior high 2-cyclohexen-1-ol selectivity in electrocatalytic cyclohexene oxidation through tailored oil–water interface

Min Li[1], Longzhou Zhang[2], Jingmin Ge[1]✉, Kaihang Sun[1], Young Dok Kim[3], Baojun Li[1], Zhongyi Liu[1], and Zhikun Peng[1]✉

[1] *Henan Institute of Advanced Technology, College of Chemistry, School of Mechanics and Safety Engineering, Zhengzhou University, Zhengzhou 450001, China*
[2] *Yunnan Key Laboratory of Electromagnetic Materials and Devices, School of Materials and Energy, Yunnan University, Kunming 650091, China*
[3] *Department of Chemistry, Sungkyunkwan University, Suwon 16419, Republic of Korea*

Cite this article: *Nano Research*, **2025**, *18*, 94907787. https://doi.org/10.26599/NR.2025.94907787

ABSTRACT: Electrocatalytic conversion presents a promising alternative to conventional industrial catalysis. While aqueous-phase electrocatalysis has achieved notable advancements, oil–water immiscible systems remain challenging due to restricted reaction flux at multiphase interfaces. To address the limitation, we engineered a biphasic reaction system featuring a tailored oil–water catalytic interface in cyclohexene oxidation reaction (COR). The system employed a catalyst-loaded porous electrode as an active phase domain, enabling spatial separation of cyclohexene (organic phase) and electrolyte (aqueous phase). The tailored oil–water interface enhanced the interfacial mass transfer of substrate-catalysts and facilitated the spontaneous migration of 2-cyclohexen-1-ol into the aqueous phase, thereby streamlining product separation. Notably, polyaniline (PANI) modification on Co_3O_4 enhanced surface lipophilicity, promoting cyclohexene adsorption and accelerating the COR catalytic kinetics (Co^{3+}–O + cyclohexene–H + e^- → Co^{2+}–OH + 2-cyclohexen-1-ol). The synergistic effects of optimized interfacial engineering and catalyst functionalization achieved exceptional performance: a current density of 45 mA·cm^{-2} at 1.6 V vs. reversible hydrogen electrode (V_{RHE}), coupled with 96.2% selectivity and 82.9% Faradaic efficiency. This work establishes an innovative paradigm for electrocatalytic conversions in oil–water immiscible systems through rational interface design and catalyst surface modulation.

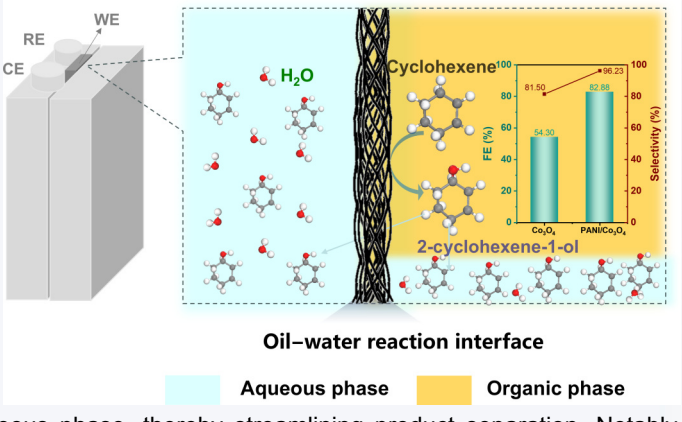

KEYWORDS: electrocatalytic cyclohexene oxidation, polyaniline (PANI)/Co_3O_4, 2-cyclohexen-1-ol, high selectivity, oil–water interface

1 Introduction

Electrocatalytic upgrading of organic molecules, utilizing clean electrons as redox equivalents to replace toxic chemical oxidants/reductants, has emerged as a transformative strategy for sustainable chemical synthesis [1–4]. This electrochemical approach demonstrates distinctive advantages, including ambient operation conditions [5], simple operation, and excellent controllability, positioning it as a pivotal technology for green chemistry and energy transition. Recent advancements in homogeneous aqueous-phase systems have achieved remarkable progress in electrocatalytic oxidation of polar substrates, such as alcohol [6–12], aldehyde [13–16], and amines [17–22]. Nevertheless, the majority of industrially relevant organic compounds display pronounced hydrophobicity, creating challenges in biphasic electrocatalysis [23–26]. The oil–water immiscibility severely restricts interfacial mass transfer, leading to suboptimal substrate-catalyst contact and consequently decreased reaction flux [27–29]. This critical limitation underscores the pressing need for innovative interfacial

Received: May 20, 2025; **Revised:** July 2, 2025
Accepted: July 10, 2025

✉Address correspondence to Jingmin Ge, yhgejingmin@163.com; Zhikun Peng, zhikunpeng@163.com

engineering strategies to enable practical electrocatalytic conversion of oil–water immiscible systems.

Recent advances in electrocatalytic conversion of oil–water immiscible systems primarily focus on the catalyst's surface modification and co-solvent utilization to improve the reaction flux (Fig. 1(a)). The reaction flux of oil–water phase could be improved by modulating the lipophilicity of catalyst surface. Such as Duan et al. synthesized $Ni(OH)_2$ modified with sodium dodecyl sulfate (SDS), improving the lipophilicity of the catalyst, which increased the yield of adipic acid by 3.6 times [30]. Besides, the reaction flux improved through adding co-solvents, such as acetonitrile (MeCN) and toluene (PhMe). Lei et al. reported that the electrochemical synthesis of 1,4-phenylenediamine, employing MeCN and PhMe as solvents and improving the system conductivity, which achieved a product selectivity of 43% at 2.25 $mA{\cdot}cm^{-2}$ [31]. Cheng et al. achieved electrooxidation of C–H of cyclohexene (Cy) using MeCN as co-solvents, improving the solubility of cyclohexene. Additionally, Pickering emulsion systems leverage particle-stabilized interfaces to amplify oil–water contact areas, showing promise in accelerating reaction kinetics for hydrophobic substrates [32]. However, the aforementioned strategies encounter three main issues: low universality of catalyst regulation strategies, high Ohmic losses, and complex reaction systems. It is urgent to develop universal, energy-efficient interfacial engineering paradigms for next-generation oil–water immiscible systems electrocatalysis.

Cyclohexene, a cornerstone platform molecule in fine chemical synthesis, exhibits complex reaction pathways during oxidation owing to its bifunctional structure containing allylic C–H [33, 34] and a conjugated C=C bond [35, 36]. While thermocatalytic oxidation currently dominates industrial production (Fig. 1(b)) [37], its application suffers from harsh conditions and limited selectivity control. However, the inherent hydrophobicity of cyclohexene poses fundamental challenges for electrochemical conversion systems, particularly in achieving efficient substrate-catalyst contact and product separation. Herein, we engineered an oil–water interface (Fig. 1(c)), which enabled compartmentalized electrooxidation of cyclohexene at the organic-electrolyte domains, while driving spontaneous phase transfer of hydrophilic 2-cyclohexen-1-ol products to the aqueous phase for continuous extraction. Further polyaniline (PANI)-coated Co_3O_4 catalysts were fabricated to enhance cyclohexene adsorption through increased surface hydrophobicity. The optimized system demonstrates exceptional performance with a low onset potential of 1.15 V vs. reversible hydrogen electrode (V_{RHE}), achieving 82.9% Faradaic efficiency (FE) and 96.2% selectivity toward 2-cyclohexen-1-ol at 1.6 V_{RHE} for cyclohexene oxidation reaction (COR).

2 Experimental

2.1 Synthesis of Co_3O_4

4.37 g of cobaltous nitrate hexahydrate ($Co(NO)_3{\cdot}6H_2O$) was dissolved in ethylene glycol ($(CH_2OH)_2$) (30 mL) and stirred for 30 min, then 0.15 g of hexadecyltrimethylammonium chloride ($(CH_3(CH_2)_{15}N(Cl)(CH_3)_3$) and 3.60 g of urea ($CO(NH_2)_2$) were added to the solution and stirred for 2 h. Then the solution was transferred to a 50 mL hydrothermal reactor and heated in an oven at 180 °C for 12 h. The precipitate was washed with water and alcohol for 3 times and dried for 12 h at 100 °C. Finally, the powders were calcined at 400 °C for 2 h at a ramping rate of 2 $°C{\cdot}min^{-1}$ and the spherical Co_3O_4 catalyst was obtained.

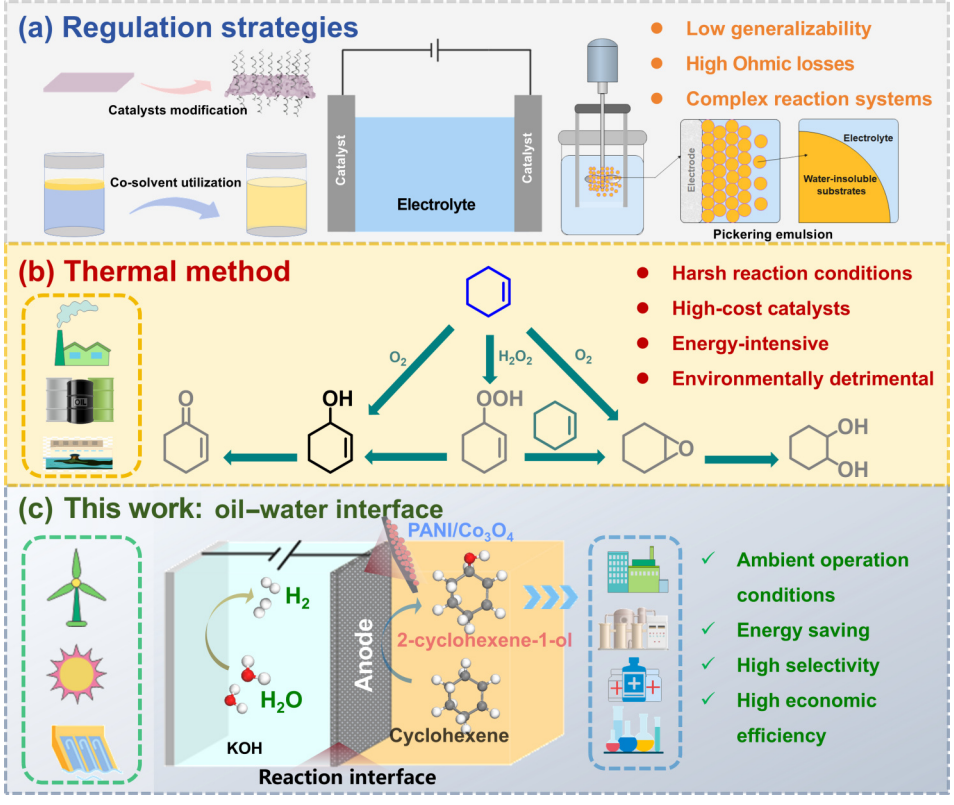

Figure 1 (a) Regulation strategies for electrocatalytic conversion of poorly water-soluble organic molecules. (b) The conventional process of thermal catalytic oxidation of cyclohexene. (c) Electrocatalytic cyclohexene oxidation through tailored oil–water interface in this work.

2.2 Synthesis of polyaniline

Hydrochloric acid (HCl) was added to 1.5 mL of aniline ($C_6H_5NH_2$) to adjust the pH to 1–2. The solution was stirred for 1 h, then 0.36 g ammonium persulphate $(NH_4)_2S_2O_8$ was added, and the mixture was reacted at room temperature for 24 h. After washing and drying, the PANI was obtained.

2.3 Synthesis of PANI/Co_3O_4

The preparation procedure for PANI/Co_3O_4 was analogous to that of PANI. Specifically, 300 mg of Co_3O_4 was introduced into the solution during the PANI synthesis process. After washing and drying steps, polyaniline-coated Co_3O_4 was successfully obtained.

2.4 Performance test conditions

The performance tests of the samples were conducted using a specific-cell (Fig. 1(c)). The cell was divided into two parts, an organic cavity and an electrolyte cavity, and the working electrodes were sandwiched between the two chambers. The performance tests were also carried out in an H-cell separated by a Nafion 117 proton membrane. All electrochemical performance tests of the catalysts were determined in a Shanghai Chenhua electrochemical workstation (model: CHI660E) using a standard three-electrode system. The scan rate of linear scanning voltammetry (LSV) was 5 mV·s^{-1}. The electrochemical impedance spectroscopy (EIS) was tested in the frequency range of 0.01–10^5 Hz at 10 mA·cm^{-2}.

2.5 Product analysis

The products were analyzed by gas chromatography (GC), GC mass spectrometry (GC-MS), and nuclear magnetic resonance (NMR). After reaction, the product was analyzed using GC-MS to identify production and conduct further quantitative analysis.

The organic phase product was analyzed using GC. The aqueous reaction product was analyzed by NMR analysis employing water suppression techniques. The electro-catalytic oxidation of cyclohexene was investigated through a three-electrode system. To address the inherent insolubility of cyclohexene in conventional electrolytes, PANI-coated Co_3O_4 was designed to optimize substrate adsorption via tailored surface hydrophilicity. As illustrated in Fig. 2(a), PANI/Co_3O_4 demonstrated a marginal current density enhancement relative to pristine Co_3O_4 at identical potentials in an H-cell, and both catalysts exhibited limited current densities. This result suggested that PANI incorporation moderately improved charge transfer kinetics while failing to improve the low FE. Interfacial wettability analysis (Fig. 2(b)) revealed a substantial water contact angle increase from 17.5° (Co_3O_4) to 82.8° (PANI/Co_3O_4), confirming reduced surface hydrophilicity post-PANI modification. Conversely, the cyclohexene contact angle decreased markedly from 25.4° (PANI/Co_3O_4) to 10.7° (Co_3O_4), demonstrating enhanced lipophilic interactions after PANI modification. These wettability transitions proved the strengthened cyclohexene adsorption capacity of the PANI/Co_3O_4 composite. To further address solubility limitations, acetonitrile was introduced as a co-solvent in the electrolyte system. LSV curves show that the current density of PANI/Co_3O_4 was slightly larger than that without acetonitrile in the electrolyte during the COR process (Fig. 2(c)). Figure 2(d) shows that the FE in the electrolyte containing acetonitrile was slightly higher than that without acetonitrile at 1.3–1.8 V_{RHE} during the COR process. The results proved that adding co-solvent to electrolyte could not effectively improve the performance of COR.

3 Results and discussion

To address the FE limitations of cyclohexene oxidation, an oil–water interface was engineered (Fig. 1(c)) to enable catalytic conversion through optimized cyclohexene-catalyst contact at the interface. Electrochemical test results revealed comparable onset potentials (1.15 V_{RHE}) for both PANI/Co_3O_4 and Co_3O_4 during the COR (Fig. 2(e)). Notably, the designed interfacial system demonstrated superior current densities for both catalysts compared to conventional H-cell during COR. While the current densities of Co_3O_4 and PANI/Co_3O_4 were small, both in the H-cell and the designed oil–water interface at 1.6 V_{RHE} during oxygen evolution reaction (OER) process. These results demonstrated the oil–water interface's effectiveness in enhancing COR efficiency while suppressing competing OER processes. Compared with Co_3O_4, the current density of PANI/Co_3O_4 was about 60 mA·cm^{-2} at 1.8 V_{RHE}, which was much higher than that of Co_3O_4 (31 mA·cm^{-2}). This improvement was attributed to PANI-mediated enhancement of cyclohexene adsorption and enrichment on the catalyst surface. Tafel plots further confirmed accelerated COR kinetics for PANI/Co_3O_4. Tafel slope value of PANI/Co_3O_4 was 108 mV·dec^{-1}, faster than that of Co_3O_4 (135 mV·dec^{-1}), which demonstrated that the introduction of PANI into PANI/Co_3O_4 enhanced its kinetic rate COR (Fig. S1 in the Electronic Supplementary Material (ESM)). The synergistic design of the oil–water interface and the hydrophobic surface of the catalyst had collectively enhanced the performance of the COR. A current density of 45 mA·cm^{-2} was achieved at 1.6 V_{RHE} with a product selectivity of 96.2% and a FE of 82.9%, representing a 19.1-fold improvement over conventional biphasic systems (Fig. 2(f)).

In addition, EIS measurements were performed on PANI/Co_3O_4 and Co_3O_4 to investigate the charge transfer behavior at the electrode/electrolyte interface. The Nyquist plot demonstrated that the semicircular-arc radius of PANI/Co_3O_4 was smaller than that of pristine Co_3O_4, suggesting it had a more efficient interfacial charge transfer (Fig. S2 in the ESM). In addition, when the double-layer capacitance (C_{dl}) of the two catalysts was tested, it was also observed that PANI/Co_3O_4 was greater than Co_3O_4, indicating that the addition of PANI enhanced the activity of Co_3O_4 (Fig. S3 in the ESM). The prepared samples were characterized by X-ray diffraction (XRD) (Fig. S4 in the ESM). The diffraction peaks located at 11.41°, 22.97°, 33.5°, 34.42°, 38.99°, 45.98°, 59.93°, 61.25°, and 65.13° belonging to the (003), (006), (101), (012), (015), (018), (110), (113), (116), and (119) crystal planes of Co_3O_4 (PDF#43-1001), indicating the successful synthesis of Co_3O_4. It can be seen from the XRD results that the diffraction peaks of PANI/Co_3O_4 corresponding to the characteristic peaks of cobalt oxide have not changed, indicating that the encapsulation of PANI has not altered the crystal structure of cobalt oxide. Meanwhile, the peak at 25.2° can correspond to the characteristic peak of PANI, indicating that PANI was successfully encapsulated. The scanning electron microscopy (SEM) image of Co_3O_4 shows that the catalyst was uniformly spherical (Fig. S5(a) in the ESM). PANI was uniformly wrapped around the outer layer of Co_3O_4 (Fig. S5(b) in the ESM). High-resolution transmission electron microscopy (HRTEM) images show that the lattice fringe of 0.52 nm corresponds to the (111) crystallographic plane of Co_3O_4 (Fig. S6(c) in the ESM). The mapping shows that the Co and O elements were evenly distributed throughout the material, which proved the successful preparation of Co_3O_4 (Figs. S6(d)–S6(f) in the ESM).

The products of COR were analyzed by GC-MS (the organic

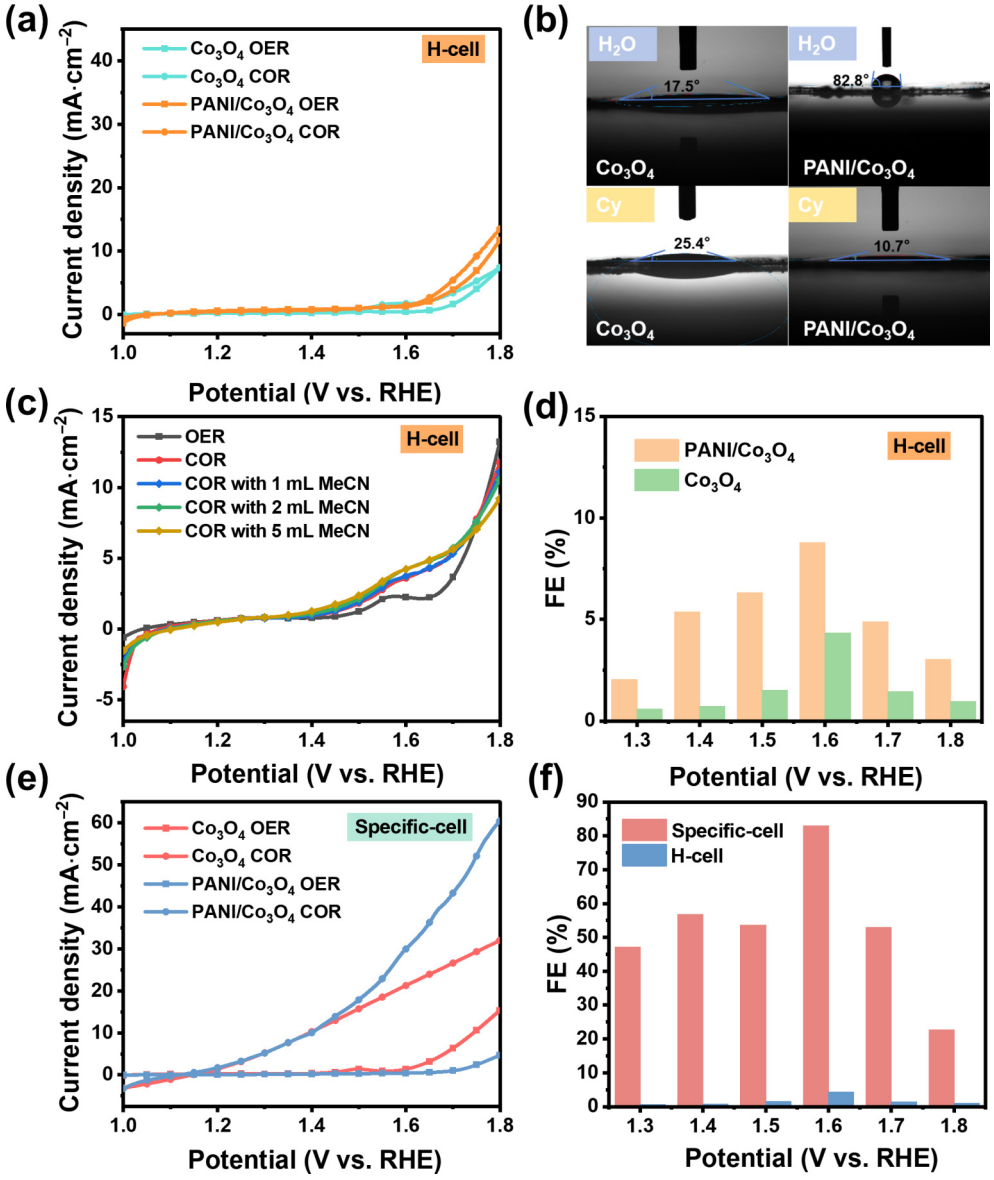

Figure 2 (a) LSV curves of Co_3O_4 and PANI/Co_3O_4 catalysts in H-cell. (b) Contact angle tests of Co_3O_4 and PANI/Co_3O_4 catalysts with water and cyclohexene. (c) LSV curves of PANI/Co_3O_4 under the condition of adding different amounts of acetonitrile in H-cell. (d) FE of Co_3O_4 and PANI/Co_3O_4 catalysts at different potentials in an H-cell (e) LSV curves of Co_3O_4 and PANI/Co_3O_4 in specific-cell. (f) FEs of PANI/Co_3O_4 at different potentials in H-cell and specific-cell.

phase products) and NMR (the aqueous phase products) at 1.3–1.8 V_{RHE}. For the NMR results, since 2-cyclohexen-1-ol was the only product present in large quantities, a separation peak was identified at 1.5–2.1 ppm, a calibration curve was constructed, standardized to the dimethyl sulfoxide (DMSO) peak, and a series of solutions of 2-cyclohexen-1-ol were prepared in 0.5 mL of electrolyte (1 M KOH). The standard nuclear magnetic resonance spectra of 2-cyclohexen-1-ol, the post-reaction nuclear magnetic resonance spectra, and the plotted calibration curves are shown in Figs. S7 and S8 in the ESM. The GC-MS results show that the products of COR were cyclohexene oxide, 2-cyclohexen-1-ol, 2-cyclohexen-1-one, and cyclohexanone (Fig. S9 and S10 in the ESM). Figure 3 shows the yield and FE of the products in aqueous and organic phases during the 1.3–1.8 V_{RHE}. The results indicated that the main product of this reaction was 2-cyclohexen-1-ol, which was primarily in the aqueous phase. At 1.6 V_{RHE}, the FE and yield of COR reached the maximum values. In the aqueous phase I (Figs. 3(a) and 3(b)), the FE of cyclohexene derivatives reached 50.9%, with the FE of 2-cyclohexen-1-ol product being 48.4%, and the selectivity being 95.2%. In aqueous phase II (Figs. 3(c) and 3(d)), the FE of cyclohexene derivatives was 35.0%, with the FE and selectivity of 2-cyclohexen-1-ol being 34.2% and 97.9%. In the organic phase (Figs. 3(e) and 3(f)), the FE of cyclohexene derivatives was 0.3%, with the FE and selectivity of 2-cyclohexen-1-ol being 0.3% and 87.7%. The results demonstrated that the products were mainly distributed in aqueous phase, which was beneficial to improve the selectivity during the COR process and simplified the separation of products.

The FE and products produced of 2-cyclohexen-1-ol obtained by PANI/Co_3O_4 during the COR process were 82.9% and 0.18 mmol, much higher than that of Co_3O_4 (54.3% and 0.13 mmol) at 1.6 V_{RHE} (Figs. 4(a) and 4(b)). The cyclic tests demonstrated that both Co_3O_4 and PANI/Co_3O_4 exhibited excellent cyclic stability during COR (Fig. 4(c)). The selectivity approached 96.2%, and the formation

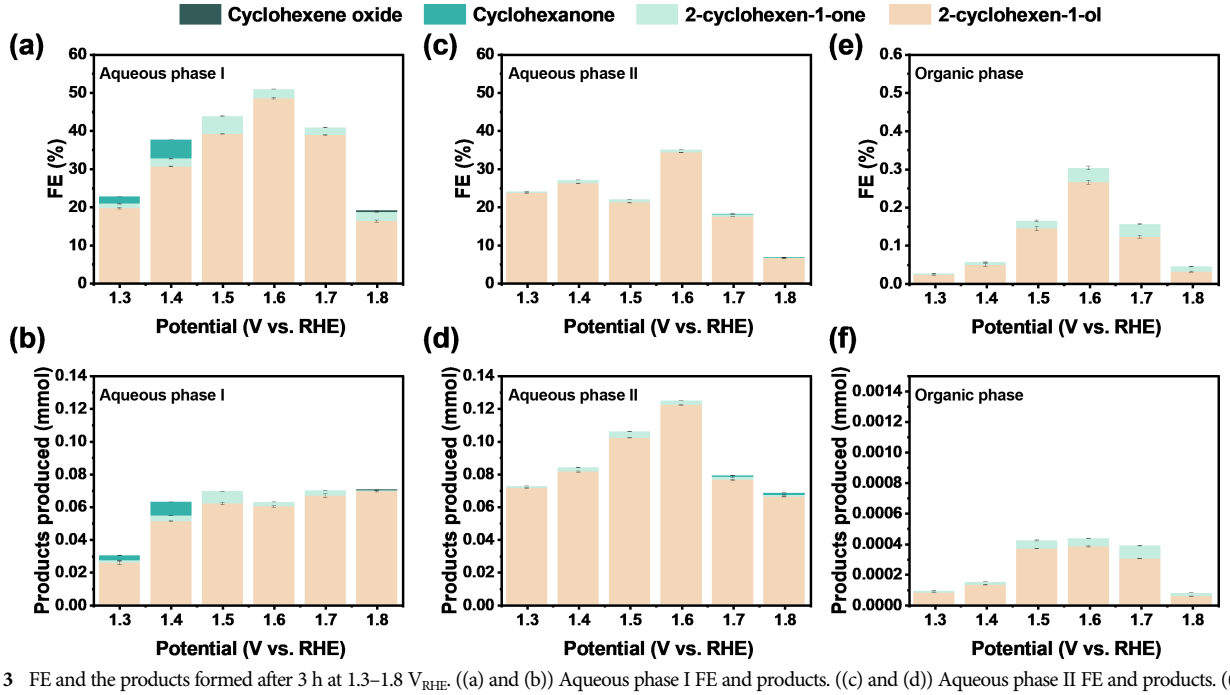

Figure 3 FE and the products formed after 3 h at 1.3–1.8 V_{RHE}. ((a) and (b)) Aqueous phase I FE and products. ((c) and (d)) Aqueous phase II FE and products. ((e) and (f)) Organic phase FE and products. All experimental points were run in triplicate and error bars indicate one standard deviation.

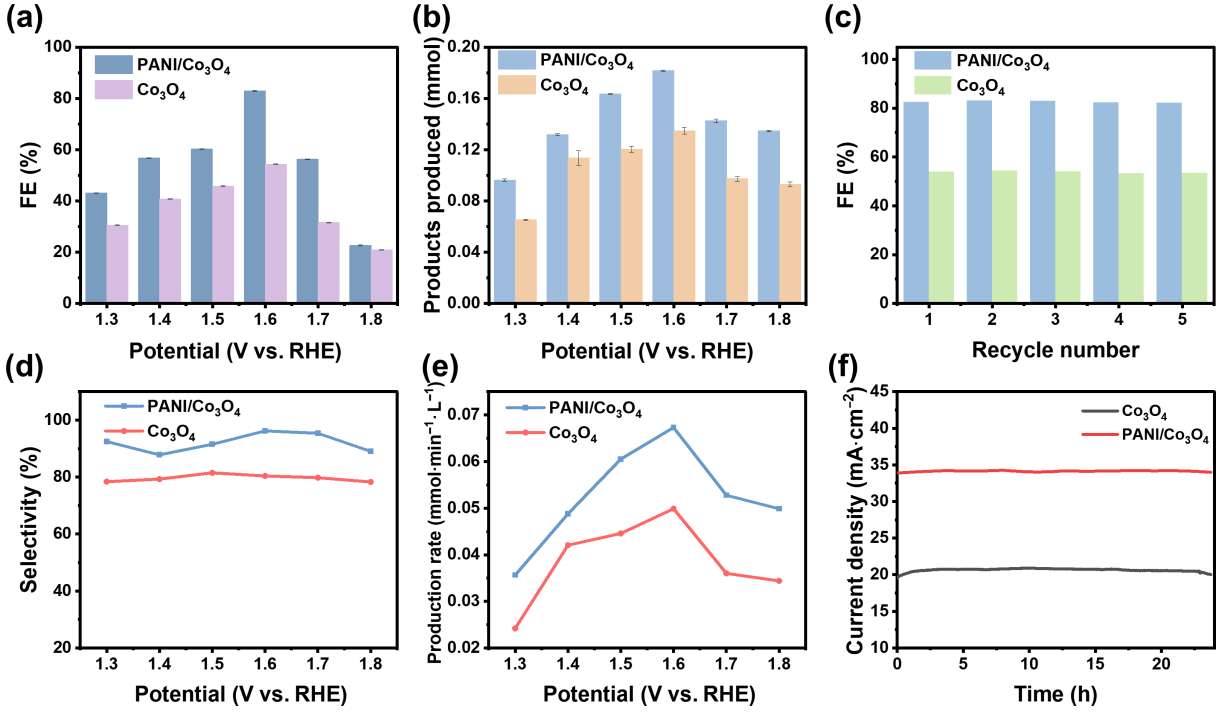

Figure 4 (a) FEs of Co_3O_4 and PANI/Co_3O_4 at different potentials. (b) The products produced of 2-cyclohexene-1-alcohol at different potentials. (c) FE of Co_3O_4 and PANI/Co_3O_4 cycling tests at 1.6 V_{RHE}. (d) Selectivity of Co_3O_4 and PANI/Co_3O_4 at different potentials. (e) Production rate of Co_3O_4 and PANI/Co_3O_4 at different potentials. (f) Chronoamperometry curves of Co_3O_4 and PANI/Co_3O_4 at 1.6 V_{RHE}.

rate reached 0.067 $mmol^{-1}·L^{-1}$, which was higher than Co_3O_4 (selectivity: 81.5% and formation rate: 0.049 $mmol^{-1}·L^{-1}$), indicating that the PANI could increase the COR performances (Figs. 4(d) and 4(e)). The long-term stability was evaluated by chronoamperometry. Figure 4(f) revealed that chronoamperometry curves of Co_3O_4 and PANI/Co_3O_4 were not attenuated, indicating that the catalysts possessed excellent long-term stability. Compared with the reported electrocatalytic oxidation of cyclohexene, PANI/Co_3O_4 is a COR catalyst with low potential, good stability and high selectivity. Its COR activity exceeds that of the reported catalysts. Compared with existing studies on the (photo) electrocatalytic oxidation of cyclohexene, PANI/Co_3O_4 demonstrated superior performance in the designed oil–water interface system, exhibiting advantages of low potential, high stability, and enhanced selectivity (Table S1 in the ESM).

The structural evolution of the Co_3O_4 was investigated during

the COR and OER. The evolution of the catalyst and the reactants kinetics on the electrode surface were studied by *in-situ* EIS during COR process. The high-frequency (HF) region was related to the redox reactions of the electrode itself, while the low-frequency (LF) region is associated with the redox reactions at the interface between the electrode and organic molecules [38]. The HF range (10–10^5 Hz) was associated with the electrooxidation of OH^- to OH* (* + OH^- → * + e^-) and the electrooxidation of electrode materials. The LF range (0.1–10 Hz) was associated with the OER process [39, 40]. The *in-situ* EIS during OER process below 1.60 V_{RHE} revealed peaks associated with the electrooxidation of electrode materials, and above 1.6 V_{RHE} belonged to the electrooxidation (Fig. 5(a)). Figure 5(b) shows that the peaks below 1.2 V_{RHE} belonged to the electrooxidation of the electrode material (Co^{2+}–O – $e_{circuit}^-$ = Co^{3+}–O). The peaks at 1.20–1.60 V_{RHE} belonged to high efficiency COR (Co^{3+}–O + cyclohexene–H + $e_{circuit}^-$ = Co^{2+}–OH + 2-cyclohexen-1-ol). The COR and OER simultaneously occurred above 1.60 V_{RHE}. The structure evolution of the catalysts under applied potential was studied by *in-situ* Raman spectroscopy. During the OER process, the peak at 696 cm^{-1} corresponds to the symmetric A_{1g} vibration of Co–O, while the peak at 196 cm^{-1} corresponds to the F_{2g} vibration [41]. Above 1.3 V_{RHE}, a new peak appeared at 610 cm^{-1} during OER process, corresponding to CoOOH (Fig. 5(c)). During COR process, the peak value of CoOOH appeared above 1.6 V_{RHE}, which was attributed to OER intervention (Fig. 5(d)). It was inferred that CoOOH formed at 1.3–1.6 V_{RHE} participated in cyclohexene oxidation, and this potential range was the high-efficiency reaction zone during COR. The *in-situ* Raman results of PANI/Co_3O_4 and Co_3O_4 show that there were no significant changes in the characteristic peak positions of Co_3O_4 and the voltage at the CoOOH peak appears (Fig. S12 in the ESM). This indicated that PANI had no effect on the structural evolution of Co_3O_4 and the formation of the active CoOOH phase.

The composition and elemental valence states of the samples were characterized by X-ray photoelectron spectroscopy (XPS) (Fig. S13 in the ESM). As shown in Fig. 5(e), the peaks at approximately 780.4 and 795.7 eV belonged to Co^{3+}–O. The peaks associated with 781.4 and 796.3 eV were attributed to Co^{2+} [42]. Compared with the pristine sample, the Co $2p_{3/2}$ peak exhibited a positive shift of 0.2 eV during the OER process, while a negative shift of 0.3 eV occurred during the COR process. This indicated that there were changes in valence states during the reaction process [43]. Figure 5(f) shows that at 1.6 V_{RHE}, the Co^{3+}/Co^{2+} ratio of the OER was higher than that of the COR, indicating the participation of Co^{3+}–O species and reduction to Co^{2+} species during the COR process.

Multi-voltage tests were conducted to study the "electrochemical–chemical" process [44]. Firstly, an electrolytic reaction was conducted for 100 s to ensure the formation of Co^{3+}–O species at 1.6 V_{RHE}. Subsequently, the catalyst was placed in 1.0 M KOH with/without cyclohexene and reacted for 100 s. As observed in Figs. 6(a) and 6(b), the current densities of both catalysts in the H-cell were relatively small at 1.6 V. Subsequently, when reacted at the open-circuit potential (OCP) for 100 s, the Co^{3+}–O species in the catalysts were reduced to Co^{2+}–O during this process. Furthermore, it can be seen from the figures that the discharge current densities of PANI/Co_3O_4 (–9 mA·cm^{-2}) and Co_3O_4 (–8 mA·cm^{-2}) were similar. This was because during the charging process, the amount of accumulated Co^{3+}–O species on the surface of PANI/Co_3O_4 is relatively close to that on Co_3O_4. This indicated that the introduction of Co_3O_4 into PANI had a relatively small improvement on its COR performances. The current densities of PANI/Co_3O_4 and Co_3O_4 in the special-cell were approximately 8 and 35 mA·cm^{-2}, respectively (Figs. 6(c) and 6(d)). The current densities were significantly increased compared with that in the H-cell. This indicated that designed oil–water interfaces in the special-cell greatly enhanced the reaction flux of the COR. Besides, the discharge current density of PANI/Co_3O_4 (–12 mA·cm^{-2}) was

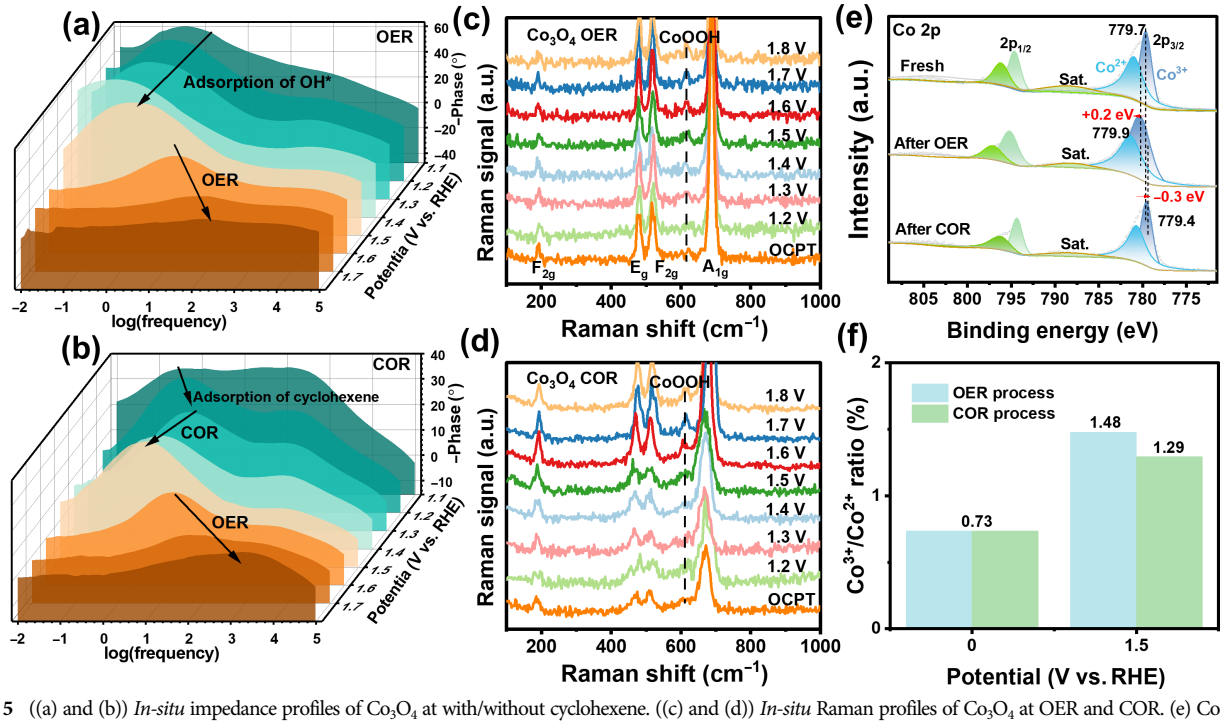

Figure 5 ((a) and (b)) *In-situ* impedance profiles of Co_3O_4 at with/without cyclohexene. ((c) and (d)) *In-situ* Raman profiles of Co_3O_4 at OER and COR. (e) Co 2p XPS profiles of Co_3O_4 initially, after OER, and after COR. (f) Ratios of Co^{3+}/Co^{2+} of the samples calculated from Co 2p XPS spectra.

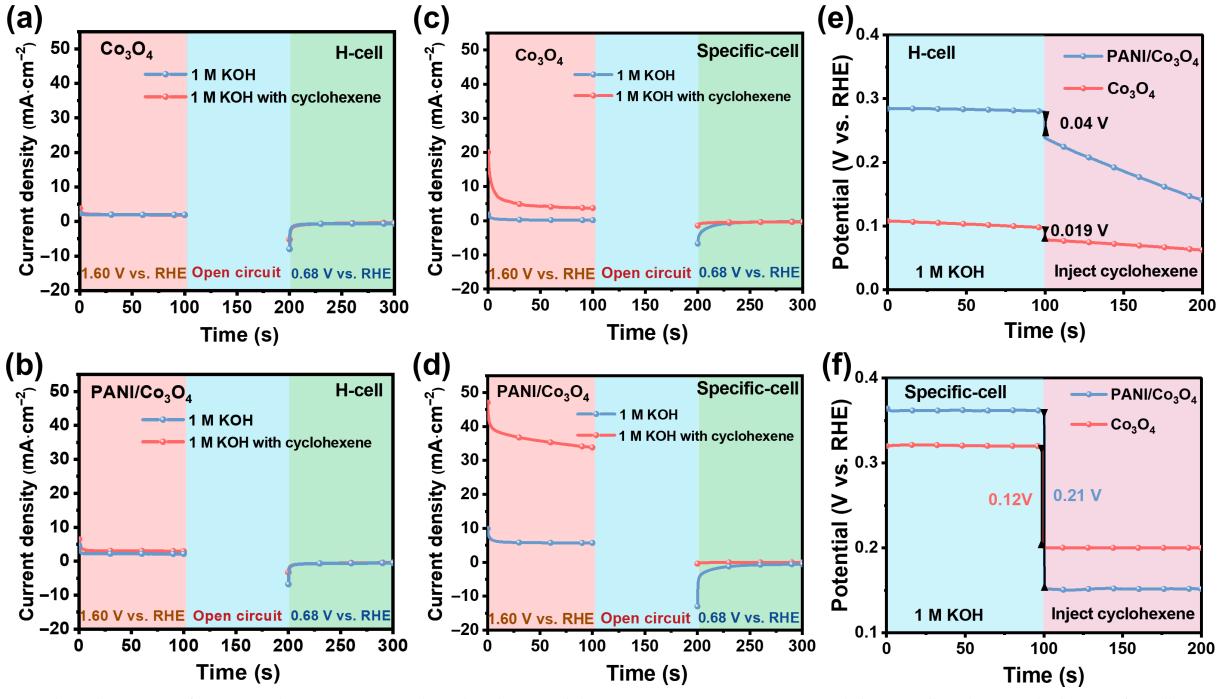

Figure 6 Multi-voltage tests of Co_3O_4 and PANI/Co_3O_4 with and without cyclohexene in 1.0 M KOH in ((a) and (b)) H-cell and ((c) and (d)) specific-cell. Open circuit potential tests of Co_3O_4 and PANI/Co_3O_4 in (e) H-cell and (f) specific-cell.

higher than that of Co_3O_4 (−7 mA·cm^{-2}) in the specific-cell without cyclohexene, indicating that much more Co^{3+}–O was accumulated on the surface of PANI/Co_3O_4. This demonstrated that introducing PANI into PANI/Co_3O_4 regulated its electronic structure, promoting the oxidation of Co^{2+}–O to Co^{3+}–O. While the discharge current densities of both catalysts were almost 0 in the specific-cell with cyclohexene, suggesting that the surface-accumulated Co^{3+}–O species were rapidly reduced to Co^{2+}–O by cyclohexene. It was indicated that the designed oil–water interface in the cell could obviously enhance the performance of COR, which was consistent with the performance test results (Fig. 2(e)). The current decreased significantly in 1.0 M KOH, whereas the current response was almost undetectable in 1.0 M KOH with cyclohexene, which indicated that the Co^{3+}–O species reacted with cyclohexene and were rapidly reduced to Co^{2+}–O species (Co^{3+}–O + cyclohexene–H + $e_{circuit}^-$ = Co^{2+}–OH + 2-cyclohexen-1-ol) and no current change was detected. This demonstrated that the designed oil–water interface effectively enhanced the reaction kinetics of COR, which was consistent with the test results (Fig. 2(f)).

To investigate the adsorption of cyclohexene on the catalysts, infrared tests were conducted on the catalyst. After the catalyst adsorbed cyclohexene, the corresponding characteristic peak of cyclohexene could be observed (Fig. S14 in the ESM). To investigate the adsorption of cyclohexene on the catalysts in the specific-cell and H-cell, the current change was tested under OCP conditions [45, 46] (Figs. 6(e) and 6(f)). A greater decrease in OCP potential indicates a stronger adsorption capacity for cyclohexene. In the specific-cell and H-cell, the OCP potential of Co_3O_4 was decreased by 0.12 and 0.019 V, while the OCP potential of PANI/Co_3O_4 was reduced by 0.21 and 0.04 V. The results demonstrated that the adsorption capacity of the catalysts for cyclohexene was obviously improved by the oil–water interface. Besides, the introduction of PANI on the Co_3O_4 could effectively improve the adsorption of cyclohexene, indicating that the adsorption of cyclohexene was effectively regulated by adjusting catalyst's hydrophilic/hydrophobic.

Density functional theory (DFT) calculations were employed to investigate the adsorption energy of cyclohexene on the samples. The construction model of Co_3O_4 and PANI/Co_3O_4 adsorbing cyclohexene is shown in Fig. 7(a). The adsorption energy of PANI/Co_3O_4 was −5.63 eV, lower than that of Co_3O_4 (−4.46 eV) (Fig. 7(b)). The results indicated that the introduction of PANI could enhance the adsorption of Co_3O_4 for cyclohexene, which was consistent with the test results (Fig. 6(f)). Based on the experimental results and *in-situ* characterizations, we formulated a hypothetical reaction mechanism (Fig. 7(c)). Under an applied voltage, tetrahedron Co^{2+}–O of PANI/Co_3O_4 was oxidized to octahedron Co^{3+}–O. The octahedron Co^{3+}–O of the prepared catalyst in the oil–water interface was reduced to tetrahedron Co^{2+}–O by the allylic C–H of cyclohexene, while cyclohexene was simultaneously oxidized to 2-cyclohexen-1-ol. The formed 2-cyclohexen-1-ol, owing to its high solubility in water, rapidly transferred to the aqueous phase, achieving spontaneous phase separation from the reactant cyclohexene.

4 Conclusions

To address the inherent limitations of oil–water immiscibility in COR, we developed a biphasic reaction system featuring a spatially confined oil–water interface that synergistically enhances mass transfer and product separation. This oil–water interface enabled direct contact between hydrophobic cyclohexene and aqueous electrolyte while facilitating spontaneous phase transfer of hydrophilic 2-cyclohexen-1-ol products into the aqueous phase, effectively facilitating product extraction. The PANI-modified Co_3O_4 catalyst demonstrated dual functionality: (1) The optimized surface hydrophobicity enhanced cyclohexene adsorption density and (2) accelerated redox cycling between Co^{2+}–OH and Co^{3+}–O active centers via proton-coupled electron transfer (Co^{2+}–OH + OH^- = Co^{3+}–O + H_2O + $e_{circuit}^-$), lowering the onset potential to

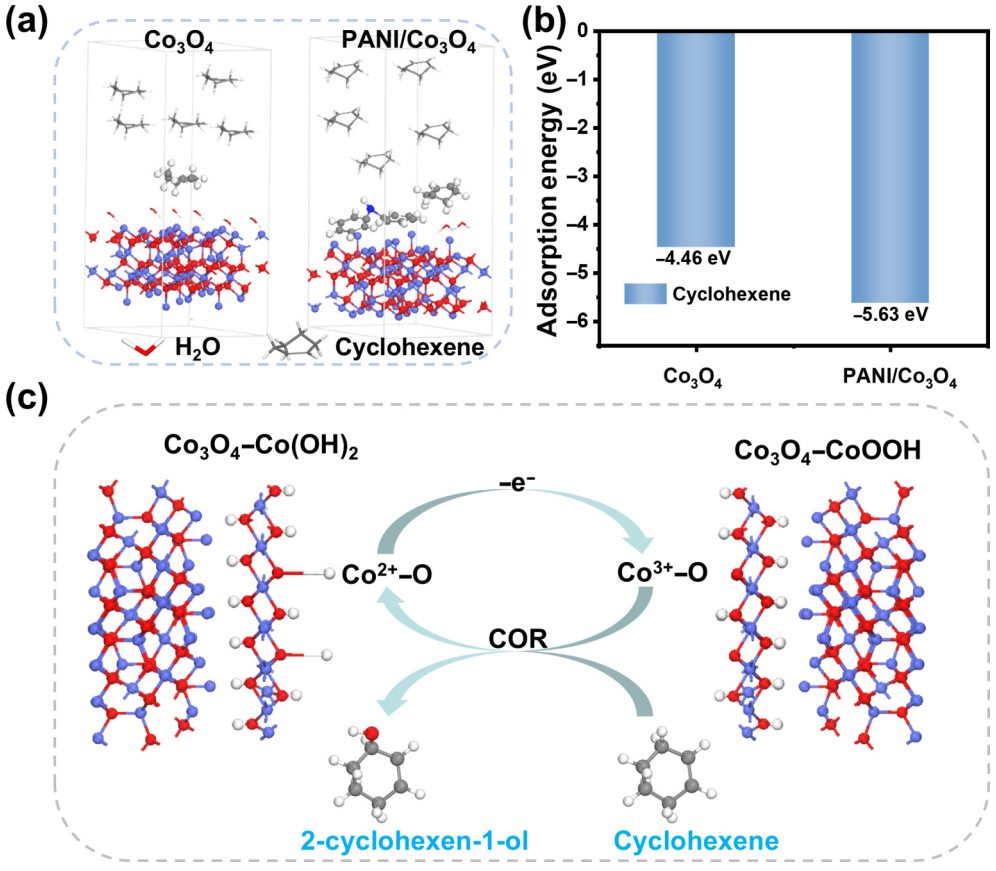

Figure 7 (a) Adsorption model diagrams of Co_3O_4 and PANI/Co_3O_4 for cyclohexene. (b) The adsorption energy of Co_3O_4 and PANI/Co_3O_4 for cyclohexene. (c) Proposed reaction pathway of cyclohexene electrocatalytic oxidation.

1.15 V_{RHE}. This accelerated the COR catalytic kinetics between cyclohexene and the catalysts (Co^{3+}–O + cyclohexene–H + e^- → Co^{2+}–OH + 2-cyclohexen-1-ol). The synergistic interplay between interface engineering and catalyst design achieved exceptional performance: 45 mA·cm^{-2} current density at 1.6 V_{RHE} with 96.2% product selectivity and 82.9% Faradaic efficiency, representing a 19.1-fold improvement over conventional biphasic systems. This work has opened an avenue for electrocatalytic conversion of water-immiscible organics through oil–water interface engineering, potentially extensible to other multiphase electrochemical systems.

Electronic Supplementary Material: Supplementary material (detailed description of experimental procedures, materials characterization data (XRD, SEM, and TEM), and spectroscopic data and fits (Raman, IR, and XPS)) is available in the online version of this article at https://doi.org/10.26599/NR.2025.94907787.

Data availability

All data needed to support the conclusions in the paper are presented in the manuscript and the Electronic Supplementary Material. Additional data related to this paper may be requested from the corresponding author upon request.

Acknowledgements

This work was supported by the National Natural Science Foundation of China (No. 22278380) and China Postdoctoral Science Foundation (Nos. 2024M762994 and GZC20232392). This study was supported by the project of Yunnan Key Laboratory of Electromagnetic Materials and Devices, Yunnan University (No. ZZ2024009). The theoretical calculations were supported by National Supercomputing Center in Zhengzhou.

Declaration of competing interest

All the contributing authors report no conflict of interests in this work.

Author contribution statement

M. L.: Data curation, formal analysis, writing – original draft. L. Z. Z.: Data curation. J. M. G.: Visualization, investigation, writing – review & editing. K. H. S., Y. D. K., B. J. L., and Z. Y. L.: Supervision. Z. K. P.: Conceptualization, funding acquisition, supervision, writing – review & editing. All the authors have approved the final manuscript.

Use of AI statement

None.

References

[1] Liu, Y. W.; Lou, Z. X.; Wu, X. F.; Mei, B. B.; Chen, J. C.; Zhao, J. Y.; Li, J.; Yuan, H. Y.; Zhu, M. H.; Dai, S. et al. Molecularly distorted local structure in Bi_2CuO_4 oxide to stabilize lattice oxygen for efficient formate electrosynthesis. *Adv. Mater.* **2022**, *34*, 2202568.

[2] Horn, E. J.; Rosen, B. R.; Baran, P. S. Synthetic organic electrochemistry: An enabling and innately sustainable method. *ACS Cent. Sci.* **2016**, *2*, 302–308.
[3] Ma, C.; Fang, P.; Liu, Z. R.; Xu, S. S.; Xu, K.; Cheng, X.; Lei, A. W.; Xu, H. C.; Zeng, C. C.; Mei, T. S. Recent advances in organic electrosynthesis employing transition metal complexes as electrocatalysts. *Sci. Bull.* **2021**, *66*, 2412–2429.
[4] Waldvogel, S. R.; Janza, B. Renaissance of electrosynthetic methods for the construction of complex molecules. *Angew. Chem., Int. Ed.* **2014**, *53*, 7122–7123.
[5] Francke, R.; Little, R. D. Redox catalysis in organic electrosynthesis: Basic principles and recent developments. *Chem. Soc. Rev.* **2014**, *43*, 2492–2521.
[6] Zhang, Q. Q.; Xia, T. Y.; Huang, H.; Liu, J. L.; Zhu, M. Y.; Yu, H.; Xu, W. F.; Huo, Y. P.; He, C. L.; Shen, S. P. et al. Autocatalytic reduction-assisted synthesis of segmented porous PtTe nanochains for enhancing methanol oxidation reaction. *Nano Res. Energy* **2023**, *2*, e9120041.
[7] Zhao, Q. Q.; Zhao, B.; Long, X.; Feng, R. F.; Shakouri, M.; Paterson, A.; Xiao, Q. F.; Zhang, Y.; Fu, X. Z.; Luo, J. L. Interfacial electronic modulation of dual-monodispersed Pt–Ni_3S_2 as efficacious Bi-functional electrocatalysts for concurrent H_2 evolution and methanol selective oxidation. *Nano-Micro Lett.* **2024**, *16*, 80.
[8] Wu, F. S.; Zeng, L.; Zhu, L. H.; Wang, W. Z.; Cao, C. H.; Yang, Z. Q.; Shang, C. X.; Ye, H. Q.; Guo, Z. X. Cooperative Pd@CoNi/rG catalyst for highly efficient and stable electrocatalytic methanol and ethanol oxidations. *Chem. Eng. J.* **2024**, *502*, 158010.
[9] Guo, R. Y.; Ji, S. D.; Liu, Y. B.; Dong, X. B.; Li, Y. R.; Liu, X.; Yang, C. L.; Zheng, Y. Z.; Jin, M. S. Facile synthesis of PtP_2 nanocrystals as highly active electrocatalysts for methanol oxidation. *ACS Appl. Mater. Interfaces* **2024**, *16*, 23233–23240.
[10] Ji, D.; Huang, B. Y.; Li, H. W.; Guo, P.; Li, W. P.; Liu, R.; Zhao, X. H.; Li, G. X. Enhanced electro-catalysis for methanol oxidation reaction performance by edge defects of ordered mesoporous carbon. *J. Colloid Interface Sci.* **2025**, *683*, 68–80.
[11] Tanwar, N.; Narjinari, H.; Sharma, H.; Dhole, S.; Jasra, R. V.; Kumar, A. Electrocatalytic oxidation of methanol and ethanol with 3d-metal based anodic electrocatalysts in alkaline media using carbon based electrode assembly. *Inorg. Chem.* **2024**, *63*, 3005–3018.
[12] Wang, J.; Zhang, A.; Niu, W. X.; Liu, G. G.; Zhou, X. C.; Wang, L. X.; Liu, X. Z.; Li, L. J.; Li, Z. J.; Zhai, L. et al. 2H–Au nanosheet-templated growth of pdfe for electrocatalytic methanol oxidation. *Adv. Funct. Mater.* **2025**, *35*, 2405073.
[13] Yang, M.; Jiang, Y. M.; Dong, C. L.; Xu, L. T.; Huang, Y. T.; Leng, S. F.; Wu, Y. D.; Luo, Y. X.; Chen, W.; Nga, T. T. T. et al. A self-reactivated PdCu catalyst for aldehyde electro-oxidation with anodic hydrogen production. *Nat. Commun.* **2024**, *15*, 9852.
[14] Xie, Y. N.; Sun, L. Z.; Pan, X.; Zhou, Z. Y.; Zhao, G. H. Selective two-electron electrocatalytic conversion of 5-hydroxymethylfurfural boosting hydrogen production under neutral condition over $Co(OH)_2$–CeO_2 catalyst. *Appl. Catal. B: Environ.* **2023**, *338*, 123068.
[15] Cheng, G. H.; Zhai, Z. H.; Sun, J. M.; Ran, Y. F.; Yang, W. F.; Tan, F. Q.; Zhang, Z. H. Elucidating role of alloying in electrocatalytic hydrogenation of benzaldehyde over nanoporous NiPd catalysts. *Chem. Eng. J.* **2023**, *474*, 145631.
[16] Lu, Y. X.; Yang, L.; Jiang, Y. M.; Yuan, Z. R.; Wang, S. Y.; Zou, Y. Q. Engineering a localized electrostatic environment to enhance hydroxyl activating for electrocatalytic biomass conversion. *Chin. J. Catal.* **2023**, *53*, 153–160.
[17] Kim, T.; Park, D. I.; Kim, S.; Yadav, D.; Hong, S.; Kim, S. H.; Yoon, H. J.; Jin, K. Mechanistic investigation of electrocatalytic reductive amination at copper electrode. *Chem. Commun.* **2023**, *59*, 4818–4821.
[18] Lu, Y. X.; Yang, H. Q. Electrocatalytic selective synthesis and tandem utilization of hydroxylamine. *Sci. China Chem.* **2025**, *68*, 2786–2803.
[19] Zhu, Z. F.; Chai, K. J.; Wu, M. Y.; Li, L.; Shi, X. L.; Zhang, P. F.; Xu, W. M. Low-overpotential, self-driving Fe–Mn co-doped nickel foam for highly efficient electrocatalytic oxidation of amines to nitriles. *Appl. Surf. Sci.* **2025**, *692*, 162743.
[20] Sun, X. H.; Peng, C.; Wang, Q.; Cheng, W. D.; Lai, Z. Q.; Fan, B. A.; Gui, Y.; Yuan, L.; Guo, F. Unveiling the mechanism of thorough electrocatalytic oxidation of monoethanolamine by ultramicroelectrode and fast-scan cyclic voltammetry. *Electrochim. Acta* **2024**, *507*, 145095.
[21] Soam, P.; Tyagi, V. Investigation of electrocatalytic oxidative coupling of arylamines for the selective synthesis of azo aromatics. *J. Org. Chem.* **2024**, *89*, 14762–14769.
[22] Zhang, Y. N.; Li, S.; Zheng, W.; Wang, X. Computational design of catalysts for ammonia synthesis. *Nano Res. Energy* **2023**, *2*, e9120068.
[23] Deng, X. H.; Xu, G. Y.; Zhang, Y. J.; Wang, L.; Zhang, J. J.; Li, J. F.; Fu, X. Z.; Luo, J. L. Understanding the roles of electrogenerated Co^{3+} and Co^{4+} in selectivity-tuned 5-hydroxymethylfurfural oxidation. *Angew. Chem., Int. Ed.* **2021**, *60*, 20535–20542.
[24] Wei, Y. N.; Zhang, Y. L. Catalytic conversion of mannose to 5-hydroxymethylfurfural promoted by hydrophobic halloysite-based catalyst in biphasic system. *Appl. Clay Sci.* **2024**, *254*, 107390.
[25] Jiang, M.; Tan, J. W.; Chen, Y. Z.; Zhang, W. B.; Chen, P.; Tang, Y.; Gao, Q. S. Promoted electrocatalytic hydrogenation of furfural in a bi-phasic system. *Chem. Commun.* **2023**, *59*, 3103–3106.
[26] Zhang, C. H.; Guo, Z. W.; Tian, Y.; Yu, C. M.; Liu, K. S.; Jiang, L. Engineering electrode wettability to enhance mass transfer in hydrogen evolution reaction. *Nano Res. Energy* **2023**, *2*, e9120063.
[27] Bui, T.; Frampton, H.; Huang, S. S.; Collins, I. R.; Striolo, A.; Michaelides, A. Water/oil interfacial tension reduction—An interfacial entropy driven process. *Phys. Chem. Chem. Phys.* **2021**, *23*, 25075–25085.
[28] Zhang, M. J.; Tang, Z. Y.; Fu, W. Q.; Wang, W. Y.; Tan, R.; Yin, D. H. An ionic liquid-functionalized amphiphilic Janus material as a Pickering interfacial catalyst for asymmetric sulfoxidation in water. *Chem. Commun.* **2019**, *55*, 592–595.
[29] Guo, W. G.; Liu, X. H.; Liu, Y.; Li, C. Chiral catalysis at the water/oil interface. *ACS Catal.* **2018**, *8*, 328–341.
[30] Li, Z. H.; Li, X. F.; Zhou, H.; Xu, Y.; Xu, S. M.; Ren, Y.; Yan, Y. F.; Yang, J. R.; Ji, K. Y.; Li, L. et al. Electrocatalytic synthesis of adipic acid coupled with H_2 production enhanced by a ligand modification strategy. *Nat. Commun.* **2022**, *13*, 5009.
[31] Hu, J. Y.; Ma, R.; Hu, J. C.; Liu, X.; Liu, X.; He, H. Y.; Yi, H.; Lei, A. W. Electrochemical oxidative dehydrogenation aromatization of cyclohex-2-enone and amines to 1,4-phenylenediamine. *Green Chem.* **2024**, *26*, 4684–4690.
[32] Deberghes, A. E.; Kazour, M. J.; Notestein, J. M.; Seitz, L. C. Chlorine-mediated electrooxidation of cyclohexene at high current density in a liquid diffusion electrode reactor. *ACS Catal.* **2024**, *14*, 12128–12139.
[33] Horn, E. J.; Rosen, B. R.; Chen, Y.; Tang, J. Z.; Chen, K.; Eastgate, M. D.; Baran, P. S. Scalable and sustainable electrochemical allylic C–H oxidation. *Nature* **2016**, *533*, 77–81.
[34] Zheng, C. P.; Li, L. L.; Han, Z. C.; Li, W. J.; Wen, X. P. Effects of manganese on the antioxidant system and related gene expression levels in the “Hong Yang” kiwifruit seedlings. *Phyton-Int. J. Exp. Bot.* **2023**, *92*, 2399–2412.
[35] Cao, Y. H.; Yu, H.; Wang, H. J.; Peng, F. Solvent effect on the allylic oxidation of cyclohexene catalyzed by nitrogen doped carbon nanotubes. *Catal. Commun.* **2017**, *88*, 99–103.
[36] Zhong, W. Z.; Liu, M. Q.; Dai, J.; Yang, J.; Mao, L. Q.; Yin, D. L. Synergistic hollow CoMo oxide dual catalysis for tandem oxygen transfer: Preferred aerobic epoxidation of cyclohexene to 1,2-epoxycyclohexane. *Appl. Catal. B: Environ.* **2018**, *225*, 180–196.
[37] Petsi, M.; Orfanidou, M.; Zografos, A. L. Organocatalytic epoxidation and allylic oxidation of alkenes by molecular oxygen. *Green Chem.* **2021**, *23*, 9172–9178.
[38] Chen, W.; Xie, C.; Wang, Y. Y.; Zou, Y. Q.; Dong, C. L.; Huang, Y.

C.; Xiao, Z. H.; Wei, Z. X.; Du, S. Q.; Chen, C. et al. Activity origins and design principles of nickel-based catalysts for nucleophile electrooxidation. *Chem* **2020**, *6*, 2974–2993.

[39] Sun, Y. X.; Shin, H.; Wang, F. Y.; Tian, B. L.; Chiang, C. W.; Liu, S. T.; Li, X. S.; Wang, Y. Q.; Tang, L. Y.; Goddard, W. A. III et al. Highly selective electrocatalytic oxidation of amines to nitriles assisted by water oxidation on metal-doped α-$Ni(OH)_2$. *J. Am. Chem. Soc.* **2022**, *144*, 15185–15192.

[40] Xu, Y. J.; Li, S. Q.; Liu, L. H.; He, J. H.; Li, K.; Wang, M. X.; Zhao, S. Y.; Li, C.; Zhang, Z. B.; Zhong, X. et al. Enhanced electrocatalytic oxidation of sterols using the synergistic effect of NiFe-MOF and aminoxyl radicals. *Acta Phys.-Chim. Sin.* **2024**, *40*, 2305012.

[41] Gao, P.; Zeng, Y.; Tang, P.; Wang, Z. X.; Yang, J. F.; Hu, A. P.; Liu, J. L. Understanding the synergistic effects and structural evolution of $Co(OH)_2$ and Co_3O_4 toward boosting electrochemical charge storage. *Adv. Funct. Mater.* **2022**, *32*, 2108644.

[42] Choi, W. I.; Choi, S.; Balamurugan, M.; Park, S.; Cho, K. H.; Seo, H.; Ha, H.; Nam, K. T. Ru-doped Co_3O_4 nanoparticles as efficient and stable electrocatalysts for the chlorine evolution reaction. *ACS Omega* **2023**, *8*, 35034–35043.

[43] Yu, X.; Jin, T. K.; Wang, H. Q.; Zhang, G. Q.; Jia, W. L.; Peng, L. C.; Sun, Y.; Tang, X.; Zeng, X. H.; Yang, S. L. et al. Heterogeneously-catalyzed aerobic oxidation of furfural to furancarboxylic acid with CuO-promoted MnO_2. *Green Energy Environ.* **2023**, *8*, 1683–1692.

[44] Peng, Z. K.; Li, S. Y.; Li, R.; Sun, K. H.; Li, J. P.; Liu, Y. Y.; Liu, Z. Y.; Wang, Y. J.; Ge, J. M.; Xiang, K. A dynamic structure evolution and reaction pathway over Ni_2P for enhancement toward furfural oxidation. *Appl. Catal. B: Environ.* **2024**, *342*, 123450.

[45] Zhou, P.; Lv, X. S.; Tao, S. S.; Wu, J. C.; Wang, H. F.; Wei, X. X.; Wang, T. H.; Zhou, B.; Lu, Y. X.; Frauenheim, T. et al. Heterogeneous-interface-enhanced adsorption of organic and hydroxyl for biomass electrooxidation. *Adv. Mater.* **2022**, *34*, 2204089.

[46] Heidary, N.; Kornienko, N. Electrochemical biomass valorization on gold–metal oxide nanoscale heterojunctions enables investigation of both catalyst and reaction dynamics with *operando* surface-enhanced Raman spectroscopy. *Chem. Sci.* **2020**, *11*, 1798–1806.